Journal of Alloys and Compounds 897 (2022) 162703

Contents lists available at ScienceDirect

Journal of Alloys and Compounds

journal homepage: www.elsevier.com/locate/jalcom

A novel composite of SnO_x nanoparticles and SiO_2@N-doped carbon nanofibers with durable lifespan for diffusion-controlled lithium storage

Liyuan Ao[a], Shenyu Du[a], Jiaxuan Yang[a], Chunqiao Jin[a], Kai Jiang[a,*], Liyan Shang[a], Yawei Li[a], Jinzhong Zhang[a], Liangqing Zhu[a], Zhigao Hu[a,b,c,**], Junhao Chu[a,b,c]

[a] Technical Center for Multifunctional Magneto-Optical Spectroscopy (Shanghai), Engineering Research Center of Nanophotonics & Advanced Instrument (Ministry of Education), Department of Materials, School of Physics and Electronic Science, East China Normal University, Shanghai 200241, China
[b] Collaborative Innovation Center of Extreme Optics, Shanxi University, Taiyuan, Shanxi 030006, China
[c] Shanghai Institute of Intelligent Electronics & Systems, Fudan University, Shanghai 200433, China

ARTICLE INFO

Article history:
Received 12 August 2021
Received in revised form 29 October 2021
Accepted 7 November 2021
Available online 18 November 2021

Keywords:
SnO_x
SiO_2
Electrospin
Carbon nanofibers
Lithium-ion battery

ABSTRACT

Carbon group materials, such as Si, SiO_2, Sn and SnO_2, with high theoretical capacity as anodes for lithium ion batteries (LIBs), suffer from the poor cycling stability resulting from the huge volume variation. To overcome the defects, a novel composite of hydrothermally synthesized ultrafine SnO_x nanoparticles and SiO_2@one-dimensional (1D) N-doped carbon nanofibers (SnO_x/SiO_2@N-CNF) is fabricated by electrospinning technique. Benefiting from the unique structure design that the SnO_x and SiO_2 nanoparticles are firmly encapsulated in the N-doped carbon nanofibers (N-CNFs), the SnO_x/SiO_2@N-CNF electrode exhibits not only excellent rate performance (434 mAh/g at 2 A/g), but also remarkable long-term cycling performance (754 mAh/g at 1 A/g after 1000 cycles) as the anode of LIBs. The N-CNFs can efficiently prevent the volume expansion and the direct contact with electrolyte of SnO_x and SiO_2, as well as shorten the diffusion path of lithium ions to improve the electrical conductivity. Interestingly, owing to the synergistic effect of SnO_x and SiO_2, the diffusion-controlled redox reaction dominates the charge transfer during charge-discharge process. As a consequence, the SnO_x/SiO_2@N-CNF could be a promising anode material with the extraordinary long-term cycling performance at high current densities, and provide a novel alternative anode material for LIBs quick-acting charging technology.

1. Introduction

With the booming development of the portable electronic equipment and electric vehicle industry and the surge in demand of people, the lithium-ion battery quick-acting charging technology is in urgent demand of breakthroughs. Despite showing advantages such as high security, long lifespan, high operating voltage, high energy density and improved environmental protection, the low theoretical capacity of 372 mAh/g seriously hinders the further development of the commercial graphite anode. [1–4,5,6]. Therefore, it is one of the easiest feasible ways to seek for an appropriate electrode material with high specific capacity and long cyclic lifespan to substitute the conventional anode. Among all the candidate anode materials, carbon group materials, such as Si, SiO_2, Sn and SnO_2, with high theoretical reversible capacity, safe working potential, natural abundance, and nontoxicity, have promoted extensive efforts to design functional electrodes with nanoscale engineering for their practical application [7–10–13]. However, their extensive application is frustrated by the poor reversibility and cycling durability due to the tremendous volume variation (~ 100%–300%, graphite is only 10%) during the charging/discharging processes [14–17]. Therefore, further research and exploration should be invested in the synthesis of novel structural carbon group anode materials for LIBs.

To solve these problems, tremendous efforts have been made to promote the electrochemical properties of these carbon group materials. One promising approach is to synthesize nanocomposites with carbonaceous matrix, which could moderate the diffusion-induced strains and accommodate the volume variation caused by the lithiation/delithiation reaction [18–21]. Among all the carbonaceous matrix with different framework, one-dimensional (1D) architectures such as carbon nanotubes (CNTs) and carbon nanofibers

* Corresponding author.
** Corresponding author at: Technical Center for Multifunctional Magneto-Optical Spectroscopy (Shanghai), Engineering Research Center of Nanophotonics & Advanced Instrument (Ministry of Education), Department of Materials, School of Physics and Electronic Science, East China Normal University, Shanghai 200241, China.
E-mail addresses: kjiang@ee.ecnu.edu.cn (K. Jiang), zghu@ee.ecnu.edu.cn (Z. Hu).

https://doi.org/10.1016/j.jallcom.2021.162703
0925-8388/

(CNFs), with large surface area, enhanced carrier collection capability, short diffusion distance, and strong tolerance for pressure changes, have been regarded as one of the most prospective carbonaceous materials [22,23]. For advanced anode materials of LIBs, CNFs demonstrably show considerable application prospects on account of their unique electronic characteristics [24,25]. Electrospinning is a straightforward and versatile technique for producing CNFs, which shows advantages of simplicity, renewability, high-efficiency, and high production [26,27]. Also, electrospinning can readily prepare multicomponent fibers by dissolving suitable inorganic/organic salt in the polymer precursor [28,29]. Accordingly, it can be used to produce an effective, controllable nanocomposites of carbon group materials and CNFs, resulting in high energy density, excellent rate capability, and superior cycling stability.

There have been many reports that successfully synthesized the composites of a carbon group material, such as Si, SiO_x and SnO_x, and a carbonaceous matrix, especially graphene, which present considerable performance as anode materials of LIBs [30–33]. For instance, Xu *et al.* encapsulated SiO_2 nanoparticles into conductive graphene bubble film by a self-assembly process in solution, which presents remarkable cycling stability and rate performance on lithium storage [30]. Gao *et al.* designed a 3D layered composite of SnO_2 quantum dots and graphene framework via hydrothermal reaction, exhibiting high reversible capacity, superior rate performance and cycling stability [31]. Our previous work has reported a novel sandwich-architecture composite of Si-doped SnO_2 nanorods and reduced graphene oxide with carbon sealing, which displays outstanding rate performance, unprecedented reversible capacity, durable cyclic stability and excellent electrical conductivity [32]. However, the long-term cycles at high current densities cannot maintain since the graphene nanoarray with high surface energy can ineluctably lead to agglomeration of the Si or Sn nanoparticles. That can be attributed to the conversion-alloying reaction, where SiO_x/SnO_x first takes part in the redox reactions, and produces a homogeneous mixture of Si/Sn, Li_2O and Li silicates at nanoscale, and then the as-formed Si or Sn continues to participate in the alloying reaction with Li^+ [34]. In addition, in these works, the electron transport path cannot be shorten by simply modifying the electrode surface. As a consequence, compositing the carbon group materials with CNFs could be a more effective and feasible approach to construct advanced anode materials for LIBs.

Herein, a novel composite of hydrothermally synthesized ultrafine SnO_x nanoparticles and SiO_2 @one-dimensional (1D) N-doped carbon nanofibers (SnO_x/SiO_2 @N-CNF) was fabricated by electrospinning technique and subsequent annealing treatment. Since the SnO_x and SiO_2 with unstable structure during cycling were firmly encapsulated in the N-doped carbon nanofibers (N-CNFs), the structural stability of the composite could be significantly improved. The N-CNFs can not only prevent the volume expansion and the direct contact with electrolyte of SnO_x and SiO_2, but also improve electrical conductivity by shorten the carrier transport path. As a consequence, the SnO_x/SiO_2 @N-CNF exhibits extraordinary rate performance, remarkable long-term cycle performance at high current densities and high electrical conductivity as anode material of LIBs. Additionally, the capacitive mechanism for energy storage of the composite that the diffusion-controlled redox reaction dominates the charge transfer during charge-discharge process was also studied in this work.

2. Experimental section

2.1. Material preparation

Firstly, ultrafine SnO_2 nanoparticles were synthesized through a one-step hydrothermal process. Typically, $SnCl_4 \cdot 5\ H_2O$ (0.5 mmol) was dissolved in 50 mL deionized water under magnetic stirring. Next, 10 mL urea solution (2.5 M) was slowly added to the $SnCl_4$ solution. After stirring for 30 min, the colorless clear solution was transferred into a 100 mL Teflon-lined stainless steel autoclave and hydrothermally treated at 200 ℃ for 24 h. After cooling down to the room temperature, the white precipitation was washed by centrifugation with deionized water and ethanol for three times, respectively. Finally, the SnO_2 nanoparticles was obtained after vacuum drying at 60 ℃ for 12 h.

The SnO_x/SiO_2 @N-CNF was prepared via electrospinning process and subsequent two-step annealing treatment. Firstly, the precursor solution for electrospinning was prepared by evenly dispersing SnO_2 nanoparticles in N,N-dimethylformamide (DMF) solution of polyacrylonitrile (PAN) and polyvinylpyrrolidone (PVP). In a typical procedure, 0.1 g SnO_2 was first dispersed in 5 mL DMF under ultrasound for 2 h to obtain a uniform dispersion. Then, 0.2 g PAN and 0.2 g PVP was dissolved in dispersion under vigorously magnetic stirring at 60 ℃ for 6 h. Next, 1 mL tetraethyl orthosilicate (TEOS) was added to the solution and stirring at 80 ℃ for 1 h until completely dissolved. The precursor solution was finally gained after stirring for about 6 h at the room temperature. The precursor solution was transferred into a plastic syringe with a 21-gauge injection needle for the electrospinning process. The procedure was carried out under the flow rate of 10 μL/min at the voltage of 15 kV. The fiber products were collected with a receiver covered with aluminum foil under sustaining rotation, which was placed 15 cm away from the tip of the syringe. Before annealing, the nanofiber membrane were then dried at a suitable temperature in vacuum over night to volatilize the solvent. Finally, the SnO_x/SiO_2 @N-CNF was obtained after two step annealing process. It was first stabilized in air at 280 ℃ for 6 h with a heating rate of 2 ℃/min, and then carbonized in argon at 700 ℃ for 2 h with a heating rate of 3 ℃/min. In addition, SiO_2 @N-CNF and SnO_x@N-CNF samples were also prepared for comparison via the same method without adding SnO_2 and TEOS, respectively.

2.2. Material characterization

JEOL-JSM-6700 F was used to obtain scanning electron microscopy (SEM) images. And the transmission electron microscopy (TEM) were carried out by a FEI Tecnai G2 F20 instrument. The crystalline structure of the samples was analyzed through X-ray diffractometer (XRD) on a high Bruker D8 Advance diffractometer with Cu-K_α radiation (λ = 1.5418 Å) between a scanning range of 10°-80°. Raman spectra was measured with a 532 nm Ar-ion laser using a Jobin-Yvon LabRAM HR Evolution spectrometer. A RBD upgraded PHI-5000 C ESCA system (Perkin-Elmer) with Mg-K_α radiation ($h\nu$=1253.6 eV) was used to gain X-ray photoelectron spectroscopy (XPS). In addition, TA Instruments 2000 was employed to perform thermogravimetric analysis (TGA) and differential scanning calorimetry (DSC). The measurement was conducted in the temperature range from 30 ℃ to 900 ℃ with the heating rate of 10 ℃/min in air.

2.3. Electrochemical measurements

The electrochemical performance was characterized via assembling coin-type 2025 cells within 0.01–3 V (vs. Li^+/Li) in a glove box with Ar filled. A homogeneous N-methyl-2-pyrrolidone (NMP) slurry consisting of 80 wt% active materials, 10 wt% acetylene black, and 10 wt% polyvinylidene fluoride (PVDF) binder was firstly prepared by stirring for 3 h. Then the working electrodes were fabricated by pasting the above slurry onto the Cu foil before drying in vacuum overnight. The active materials in the electrodes had the mass loading of around 0.6–1.0 mg/cm^2. The half-batteries were assembled with metallic lithium as counter electrode, polypropylene film (celgard 2400 USA) as separator and a solution of $LiPF_6$ (1 M) in 1:1:1 in volume ratio of ethylene carbonate, dimethyl carbonate, and ethyl methyl carbonate as electrolyte. A Land CT 3001A battery tester

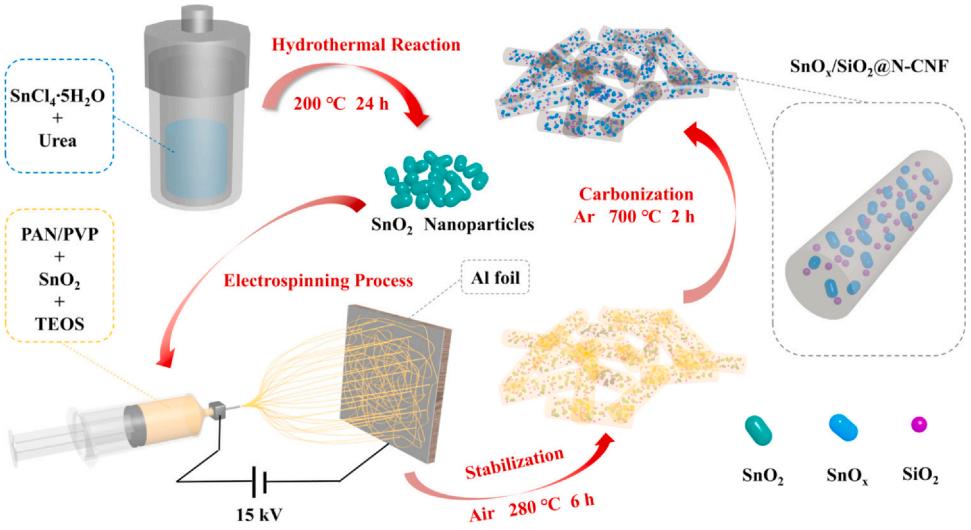

Fig. 1. The graphical synthesis procedure of SnO_x/SiO_2 @N-CNF.

was employed to implement the galvanostatic discharge-charge measurements in a voltage window of 0.01–3 V (vs. Li/Li^+). Both electrochemical impedance spectroscopy (EIS) analysis and cyclic voltammetry (CV) test were carried out on a CHI-660E electrochemical workstation.

3. Results and discussion

Fig. 1 exhibits the schematic illustration for the fabrication of the SnO_x/SiO_2 @N-CNF, which combines electrospinning and the hydrothermal synthesis technology. Firstly, the ultrafine SnO_2 nanoparticles were synthesized via a one-step hydrothermal reaction at 200 ℃ for 24 h on the basis of our previous report [32]. The electrospinning process was conducted using a precursor solution prepared by dispersing ultrafine SnO_2 and dissolving PVP, PAN and TEOS in DMF. Since the partical size of the SnO_2 nanoparticles was quite small (20–50 nm), they can be uniformly dispersed in DMF under ultrasound with little hindrance. PAN and PVP with a mass ratio of 1:1 served as the carbon precursor and provided N-doping also. To obtain the SnO_x/SiO_2 @N-CNF composite, the collected electrospun fibers were first stabilized in air at 280 ℃, while TEOS decomposed into silica nanoparticles. Then the composite was calcined at 700 ℃ in Ar for carbonization, accompanied with the reduction of SnO_2 to SnO_x. During the carbonization process, the N-CNFs were formed and served as encapsulating matrix to encapsulate SiO_2 and SnO_x nanoparticles, which can restrain the volume variation and block the direct contact with electrolyte of the nanoparticles.

The microstructure of the prepared composites were investigated by SEM and TEM. The SEM and TEM images of SnO_2 nanoparticles is displayed in Fig. 2a and e, respectively, where the particles are in the shape of rice-granular with a length of 5–10 nm. Fig. 2b-e expose the nanofibrous structures of the SiO_2 @N-CNFs, SnO_x@N-CNFs and SnO_x/SiO_2 @N-CNFs, respectively. The 1D nanofibers construction could prominently shorten the diffusion distance of Li^+, and consequently enhance the electrochemical performance [35,36]. The diameters of the fibers with a smooth surface are all in the range of 100–200 nm. Compared with Fig. 2d, the SiO_2 @N-CNF and SnO_x@N-CNF in Fig. 2b and c both exhibit the phenomenon of fiber adhesion. It is because that the silica can enhance the mechanical stiffness of the SnO_x@N-CNF [37]. Besides, it can be also found from Fig. 2f that the surface of the fibers is smooth and there are no distinct particles on the surface. For the purpose of further revealing the inner nanostructures of the SnO_x/SiO_2 @N-CNF nanocomposite, TEM and high-resolution transmission electron microscopy (HRTEM) characterization have been carried out. The results are shown in Fig. 3a-d and Fig. S2. From Fig. 3a and b, it can be inferred that the bright areas with a shape of rice-granular are ultrafine SnO_x nanoparticles with a length of 20–50 nm. Whereas the SiO_2 nanoparticles cannot be distinguished in the images, since they are in amorphous states. Fig. 3c and d show the HRTEM of the region circled in Fig. 3a and the SAED of SnO_x/SiO_2 @N-CNF, repectively, which further prove the speculation. The lattice distance of 0.279 nm in Fig. 3c accords with the (101) planes of metallic tin, and the corresponding SAED image is also displayed in the inset. To investigate into the distribution of the SnO_x and SiO_2 nanoparticles thoroughly, the HAADF elemental mapping results are provided in Fig. 3e-j. It can be indicated that all the C, N, O, Sn and Si are distributed homogeneously, which suggest the uniform distribution of SnO_x and SiO_2 nanoparticles within the N-doped carbon nanofibers.

The specific composition and crystal structure of the products were initially investigated via X-ray diffraction (XRD) analysis (Fig. 4a). For hydrothermal SnO_2 nanoparticles, the three typical diffraction peaks located at $2\theta = 26.7°$, 33.9° and 51.7° are in good agreement with the (110), (101) and (211) crystal faces of tetragonal rutile SnO_2 (JCPDS No. 41–1445), respectively. Other visible peaks are also matched with the diffraction planes. As for SnO_x@N-CNF and SnO_x/SiO_2@N-CNF, the strong diffraction peaks at the 2θ values of 30.6°, 31.9°, 43.8°, 44.9°, 62.4° and 64.6°, can be assigned to the (200), (101), (220), (111), (112) and (321) planes of metallic Sn with cubic phase (JCPDS# 65–2631), respectively. However, the peaks that accord with SnO_2 are quite weak. It could demonstrate that the rutile-type SnO_2 crystals were successfully prepared after hydrothermal reaction. However, during the calcination process, some of the SnO_2 nanoparticles were reduced to metal tin, and the others were converted into amorphous tin oxide. The broad peaks at $2\theta = 20–30°$ of SiO_2@N-CNF and SnO_x/SiO_2 @N-CNF are consistent with SiO_2 (JCPDS# 13–0026), confirming the existence of SiO_2 nanoparticles. In addition, further structural characteristics of the four samples were performed using Raman spectroscopy under 532 nm laser excitation. As shown in Fig. 4b, four obvious peaks at 478, 576, 630 and 771 cm^{-1} could be found in the spectral curve of SnO_2 nanoparticles, which are corresponding to A_{2g}, A_s, A_{1g} and B_{2g} modes of SnO_2, respectively [9,38]. However, they almost disappeared in the spectral curves of SnO_x@N-CNF and SnO_x/SiO_2 @N-CNF, which are consistent with the HRTEM and XRD results. Also, several weak silica characteristic peaks in 300–900 cm^{-1} could be observed in the spectral curves of SiO_2 @N-CNF and SnO_x/SiO_2@N-CNF [39]. Fig. 4c indicates that all the composites with N-doped carbon nanofibers deliver two

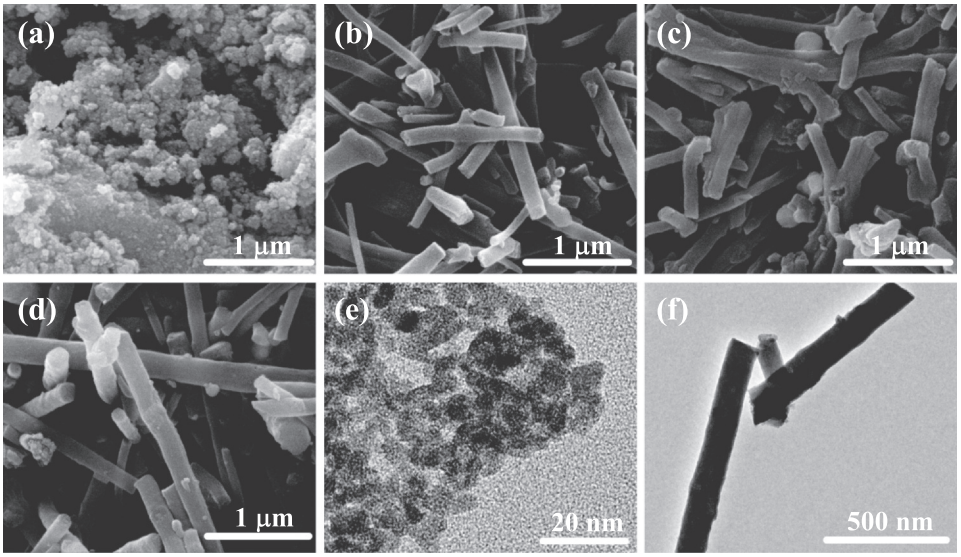

Fig. 2. High-magnification SEM images of (a) SnO_2, (b) SiO_2@N-CNF, (c) SnO_x@N-CNF and (d) SnO_x/SiO_2@N-CNF, respectively. TEM image of (f) SnO_2 (e) SnO_x/SiO_2@N-CNF.

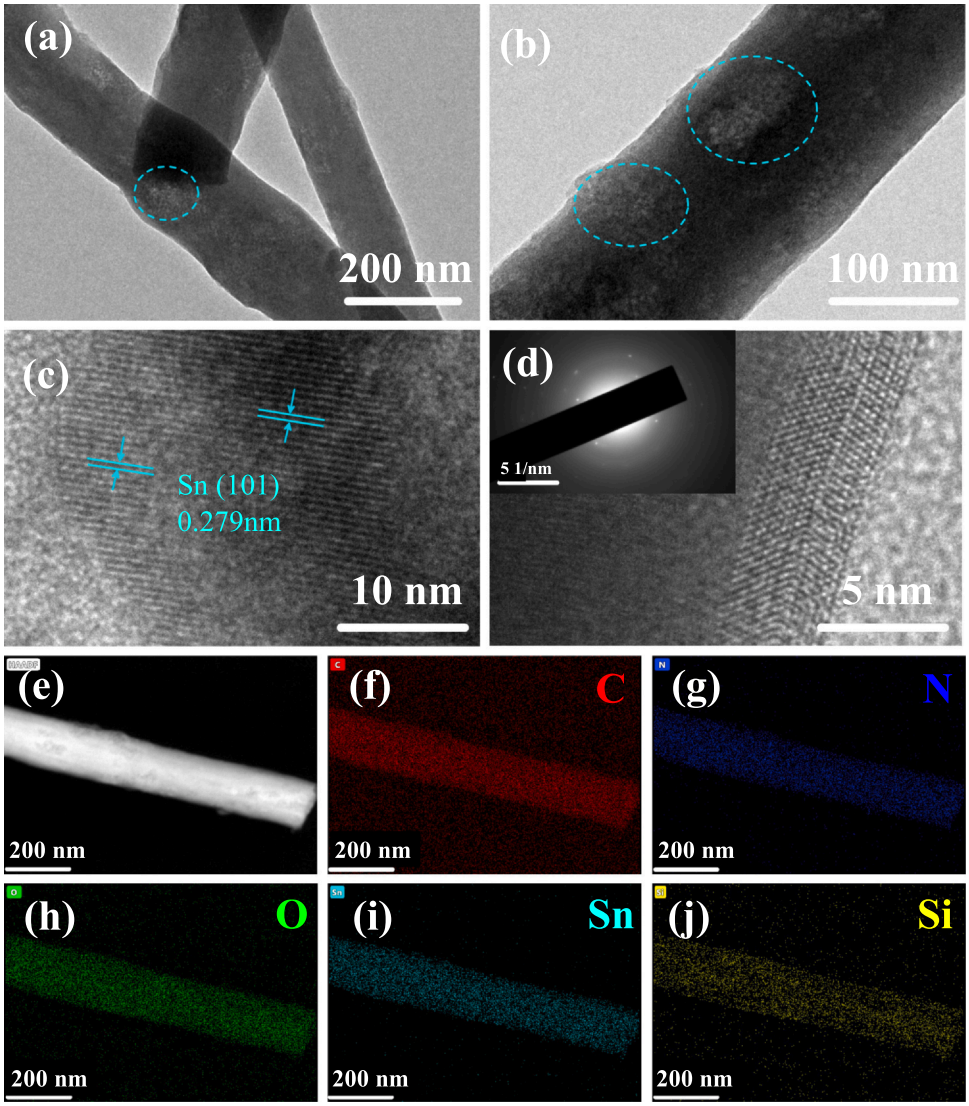

Fig. 3. (a)-(b) TEM and (c)-(d) HRTEM images of SnO_x/SiO_2@N-CNF. (e) STEM image of SnO_x/SiO_2@N-CNF composite and the corresponding elemental mapping images of (f) C, (g) N, (h) O, (i) Sn, and (j) Si, respectively.

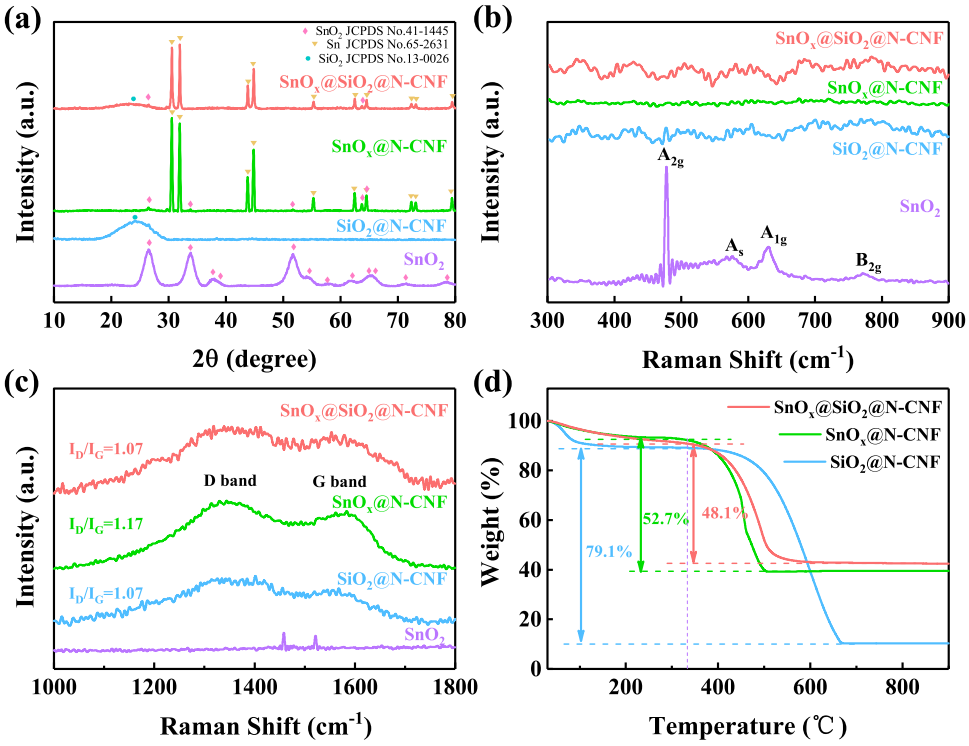

Fig. 4. (a) XRD patterns and (b)-(c) Raman spectra of the as-prepared SnO_2, SnO_x@N-CNF, SiO_2@N-CNF and SnO_x/SiO_2@N-CNF, respectively. d) TGA curves of SnO_x@N-CNF, SiO_2@NCNF and SnO_x/SiO_2@N-CNF.

peaks at 1348 and 1589 cm^{-1}, according with D band (k-point phonon of A_{1g} symmetry) and G band (E_{2g} phonon of C sp^2 atoms) of carbon, respectively [40,41]. The ratio of the intensities of D band and G band (I_D/I_G) is usually regarded as a coefficient of the disorder degree of sp^2 domains [41]. The calculated I_D/I_G value of SnO_x/SiO_2 @N-CNF is 1.07, which is equal to that of SiO_2 @N-CNF. It demonstrates that the SnO_x has almost no effect on the I_D/I_G value. However, the value is lower than the calculated I_D/I_G value of SnO_x@N-CNF (1.17), which indicates the SiO_2 can reduce the I_D/I_G value of the composites. Therefore, it can be inferred that the SiO_2 can increase the partial graphitization, and thereby reducing the introduced defects in carbon nanofibers [7]. The quite high I_D/I_G values of the three composites indicate their low degree of graphitization and high degree of disorder. It has been proved that the disordered electrode materials have high Li^+ diffusion, so all of the three electrodes have enhanced diffusion of the lithium ions during charging and discharging process [42]. Besides, the contents of C were measured by the thermogravimetric analysis, the results of which are shown in Fig. 4d. The mass decrement in 30–100 ℃ could be ascribed to the evaporation of water, while the weight loss in 335–650 ℃ is regarded as carbon burning off. For SnO_x@N-CNF and SnO_x/SiO_2 @N-CNF, the weight change in 100–335 ℃ could be attributed to the redox reaction of SnO_x. Thus, the N-CNF accounts for 79.1 wt%, 52.7 wt% and 48.1 wt% of SiO_2 @N-CNF, SnO_x@N-CNF and SnO_x/SiO_2 @N-CNF, respectively.

X-ray photoelectron spectroscopy (XPS) was employed to study the element constituent and valence state of the SnO_x/SiO_2@N-CNF. As shown in Fig. S3a, the typical peaks at 103.1, 284.8, 399.1, 486.9, 495.4 and 532.4 eV in the overall spectrum are in accordance with Si 2p, C 1s, N 1s, Sn $3d_{5/2}$, Sn $3d_{3/2}$ and O 1s, respectively. The high-solution Sn 3d spectrum (Fig. S3b) shows four fitting peaks at 495.7/487.3 eV and 495.1/486.6 eV, corresponding to Sn $3d_{3/2}$/Sn $3d_{1/2}$ of Sn^{4+} and Sn, respectively [43,44]. The results provide further evidence of the SnO_x nanoparticles. By calculating the areas of the Sn^{4+} and Sn peaks, the atomic ratio of Sn^{4+} and Sn in SnO_x/SiO_2 @N-CNF can be estimated as 1.27. The deconvoluted O 1s spectrum (Fig. S3c) was fitted into peaks located at 532.7, 532.1 and 531.1 eV, which are related to the C-O, Si-O and Sn-O bonds, respectively [45,46]. Fig. S3d displays the Si 2p spectrum, where a well-proportioned fitting peaks at 103.1 eV can be assigned to Si^{4+} [47]. Therefore, consistent with the XRD and Raman results, it has been further confirmed that the Si element exists in the composite with the form of silica. The atomic ratio of the elements in SnO_x/SiO_2 @N-CNF were also investigated via XPS analysis. The major elements C, N, O, Si and Sn are in the atomic ratio of 51.1: 7.2: 30.2: 9.2: 2.3, corresponding to the weight ratio of 35.6: 5.8: 27.9: 14.9: 15.8 wt%, which is roughly in agreement with the results of Energy dispersive X-ray analysis (EDX) and thermogravimetric analysis (TGA).

Galvanostatic discharge/charge (GDC) tests in half-cells were firstly performed to estimate the electrochemical performance of the composites as anode materials of LIBs. To reveal the intrinsic electrochemical property of the SnO_x/SiO_2@N-CNF, the rate reversible capacity and cycling performance of the electrodes were measured in a potential window of 0.01–3.0 V (vs. Li^+/Li). As shown in Fig. 5a, the rate capacities of the four electrodes were examined under various current densities between 0.1 A /g and 5 A/g. The SnO_x/SiO_2@N-CNF electrode delivers a specific capacity of 957, 846, 707, 552, 434 and 303 mAh/g at 0.1, 0.2, 0.5, 1, 2 and 5 A/g, respectively, which presents a remarkable advantage, as compared with other three samples. Additionally, it can obtain back to 824 mAh/g at 0.1 A/g and 752 mAh/g at 0.2 A/g after 30 cycles and 40 cycles, respectively, showing excellent reversibility. Furthermore, the SnO_x/SiO_2@N-CNF electrode delivers an ultrahigh initial specific capacity of 1435 mAh/g at 0.1 A/g in discharge process, which is almost reached the theoretical capacity value of SnO_2 or SiO_2. The corresponding discharge-charge curves are illustrated in Fig. 5c, where no apparent hysteresis growth could be observed in the discharge-charge plateaus even at high current densities. This confirms the outstanding transmission capacity of electron/ion in the SnO_x/SiO_2@N-CNF electrode. The lower capacity of SiO_2@N-CNF electrode can be ascribed to the quite

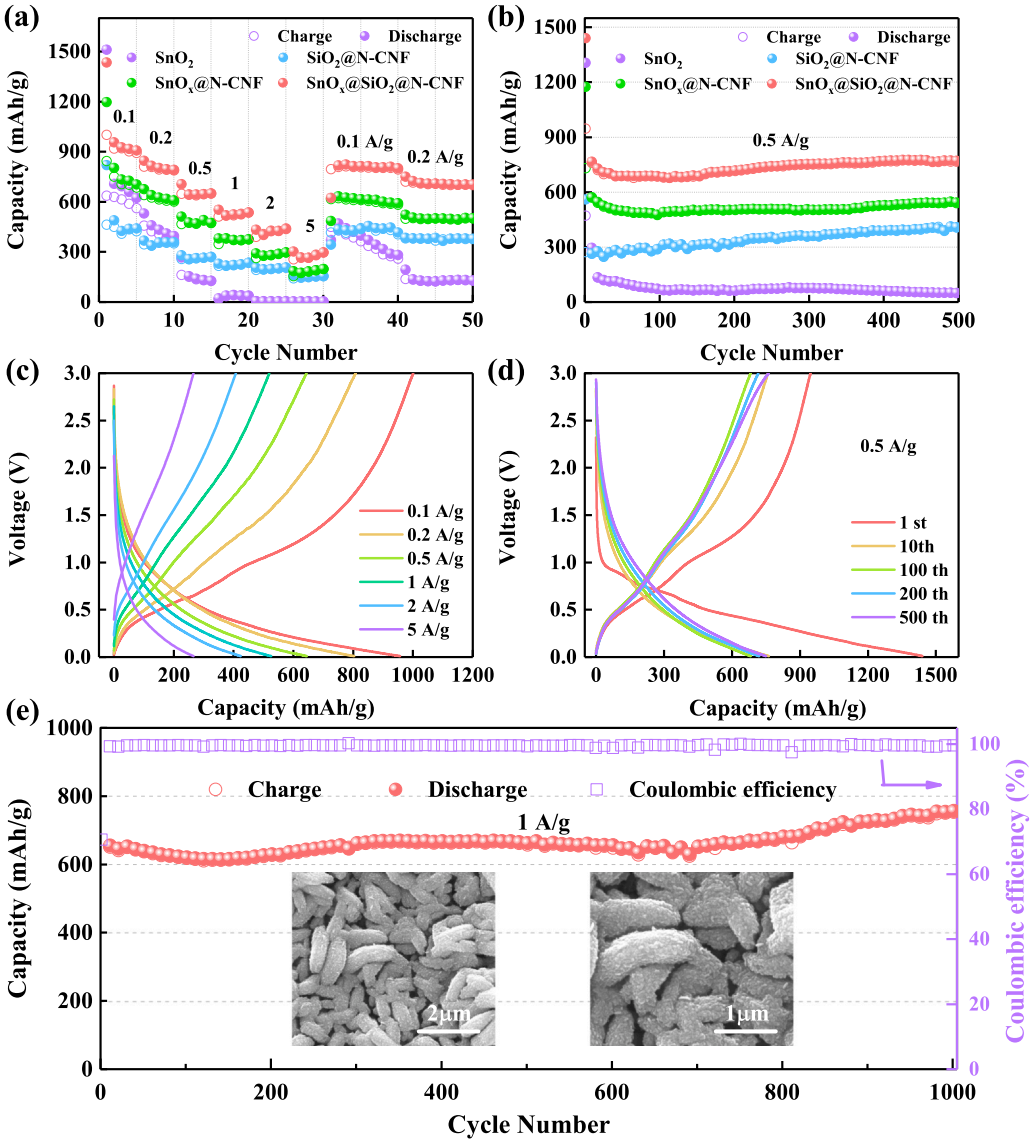

Fig. 5. Rate performance of the four composite electrodes at different current densities. (b) Cycling performance of the as-prepared samples at 0.5 A/g. The GDC profiles of the SnO_x/SiO_2@NCNF electrode (c) at the increasing discharge current density from 0.1 to 5.0 A/g and (d) for the 1st, 10th, 100th, 200th and 500th cycles at 0.5 A/g. (e) Cycling performance of the SnO_x/SiO_2@N-CNF electrode at 1 A/g, at 0.1 A/g for the first five cycles. The insets are the SEM images of the cycled SnO_x/SiO_2@N-CNF electrode after 1000 cycles at 1 A/g.

high content of carbon and the severe fiber adhesion, which can greatly reduce the surface area, and thereby reducing the lithium storage capacity. Besides, the rate capacity of the SnO_x@N-CNF electrode has the same trend with the SnO_x/SiO_2@N-CNF electrode, while the specific capacity is much lower. The electrode of pure hydrothermal SnO_2 nanoparticles with a highest initial capacity exhibits poor rate performance and reversibility. These results demonstrate that the synergistic effect of the SnO_x and SiO_2, as well as the special feature of N-CNF contribute to the improvement of rate performance. Besides, to explore the effect of the annealing temperature to the electrochemical performance of the SnO_x/SiO_2 @N-CNF electrode, a compared sample with an annealing temperature of 600 °C in Ar was prepared and named SnO_x/SiO_2@N-CNF-600. The comparison of the rate performance with the product SnO_x/SiO_2 @N-CNF (SnO_x/SiO_2@N-CNF-700) electrode is exhibited in Fig. S4, indicating that the reversible capacity and rate performance cannot be obviously improved at the annealing temperature of 600 °C.

Aiming at analyzing the cyclic stabilities during continually charge/discharge process of the SnO_x/SiO_2@N-CNF as anode material of LIBs, the galvanostatic cycling results at 0.5 A/g and 1 A/g in the voltage of 0.01–3.0 V (vs. Li^+/Li) are presented in Fig. 5b and e, respectively. As shown in Fig. 5b, a capacity reduction emerges in the first 40 cycles for all the four samples, owing to the undulation of the solid electrolyte interface (SEI) layer and the thermal decomposition of electrolyte. The specific capacities of the electrodes with N-CNF maintain steady within a certain range due to the stable internal structure. Also, they show slight increase because the unique 1D structure of the N-CNFs can shorten the Li^+ diffusion path, and the distance would be further shortened with the cycling process [26]. Without the cladding of N-CNF, agglomeration of particles and side reactions with electrolyte occurs on the pure SnO_2 electrode, resulting in capacity decaying [36]. With the capsulation of N-CNF and synergistic effect of SiO_2 and SnO_x, the specific capacity of the SnO_x/SiO_2@N-CNF electrode remains 750 mAh/g after 500 cycles at 0.5 A/g and 754 mAh/g 1 A/g (Fig. 5e) after 1000 cycles, which is much higher than other samples and most reported carbon group based materials. Note that the increase of the capacity between 800 and 1000 cycles may be due to the increase of the temperature in the test room. Moreover, the initial coulombic efficiency of the SnO_x/SiO_2 @N-CNF electrode is 70.7% at 0.1 A/g and 65.8% at 0.5 A/g, which

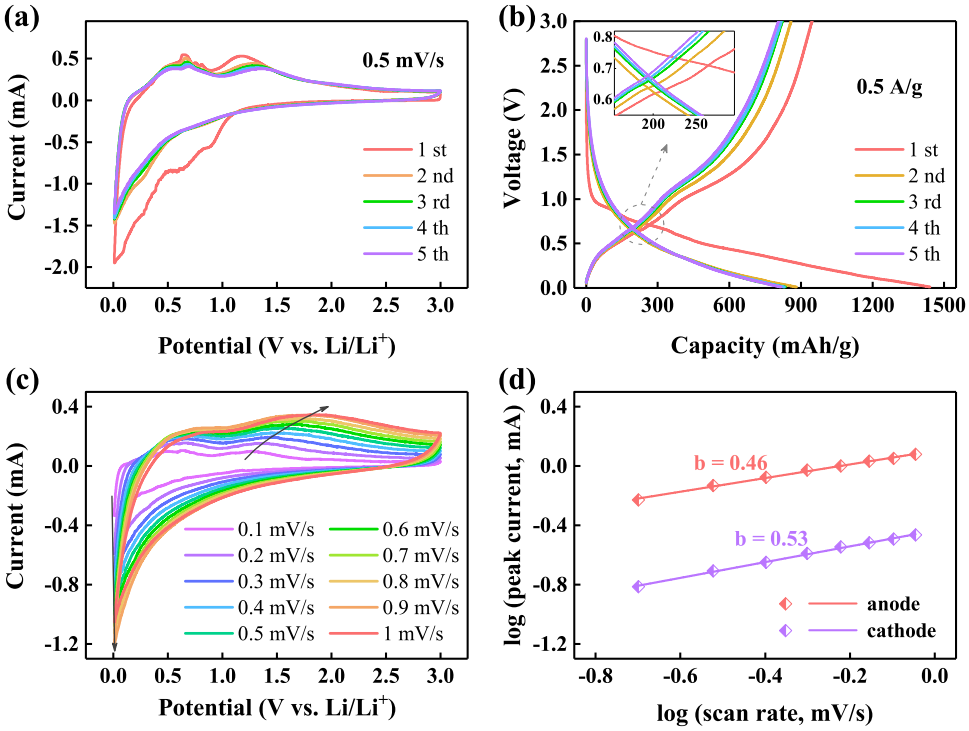

Fig. 6. (a) CV curves at a scan rate of 0.5 mV/s in the range of 0.01-3.0 V vs. Li/Li+, (b) the GDC profiles of SnO_x/SiO_2@N-CNF electrode for the first five cycles, (c) CV curves at various rates from 0.1-1 mV/s and (d) the fitted specific anodic/cathodic peak current for determining the b value of SnO_x/SiO_2@N-CNF electrode, respectively.

increases to 96.9% after one cycle and then maintains over 99% at 1 A/g after the first five cycles at 0.1 A/g. The corresponding discharge-charge curves at the current density of 0.5 A/g are displayed in Fig. 5d. The charge curves of the first and tenth cycles exhibit the similar shape with capacity decline, while the 100 th to 500 th charge-discharge curves present great doublication, further proving the outstanding cycling stability of SnO_x/SiO_2@N-CNF as anode of LIBs. The SEM images of the four cycled electrodes after 500 cycles at 0.5 A/g are shown in Fig. S7. It can be seen from Fig. S7a that the SnO_2 electrode shows severe particle aggregation. There are many ultrafine grains on the surface of the fibers for the cycled SiO_2@N-CNF electrode, which could be the products of the side reaction during cycling process. The SnO_x@N-CNF and SnO_x/SiO_2@N-CNF electrodes show great structure stability even after 500 cycles, as shown in Fig. S7c and d, respectively. The 1D fibrous structure is clearly visible especially for the cycled SnO_x/SiO_2@N-CNF electrode, which could further confirm the enhanced structure stability of SnO_x/SiO_2@N-CNF after repeated lithium insertion-extraction process. Also, the cycling stability of the SnO_x/SiO_2@N-CNF electrode is better than SnO_x/SiO_2@N-CNF-600 at 0.5 A/g as shown in Fig. S5. It demonstrates that the annealing temperature of 700 °C is prerequisite to gain a more stable structure of SnO_x/SiO_2@N-CNF. Besides, the SEM images of the cycled SnO_x/SiO_2@N-CNF electrode after 1000 cycles at 1 A/g were displayed in Fig. 5e. As shown in the insets, the SnO_x/SiO_2@N-CNF electrode could maintain the perfect 1D fibrous structure even after repeating 1000 lithium insertion-extraction process.

To explore the inherent reaction mechanism of the lithiation/delithiation process for SnO_x/SiO_2 @N-CNF electrode, cyclic voltammetry (CV) test was performed at a potential of 0.01–3.0 V vs. Li/Li^+. Fig. 6a exhibits the first five cycles of the CV curves of SnO_x/SiO_2 @N-CNF electrode. The 1–5 cyclic CV curves and the corresponding the GDC profiles are displayed in Fig. 6a and b, respectively. In the initial lithium insertion (cathodic) scan, two reduction peaks at 0.58 and 0.88 V could be observed, which are related to the irreversible reactions between the electrode and electrolyte and the reduction of SnO_2 ($SnO_2 + 4Li^+ + 4e^- \rightarrow Sn + 2Li_2O$) and SiO_2 ($2SiO_2 + 4Li^+ + 4e^- \rightarrow 2Si + Li_4SiO_4$) [45,47]. The small peaks at 0.10, 0.28 and 0.39 V are corresponding to the multistep formation reaction of $Li_{4.4}Sn$ alloys ($Sn + xLi^+ + xe^- \leftrightarrow Li_xSn$, $x \leq 4.4$) [48]. In the 2–5 cycles, the peaks at 0.58 and 0.88 V disappeared due to the irreversible formation of the SEI film on the surface of the anode materials. Also, the three peaks in 0.1–0.4 V still exist, but become weaker. The weak and broad peak at 0.78 V can also be linked with the conversion of SnO_2 to Sn/Li_2O, while the position shifts under the impact of the SEI film. The positions of the reduction peaks of SiO_2 are almost coincide with SnO_2, so they cannot be distinguished in the curves. As for lithium deintercalation (anodic) scan, four evident oxidation peaks corresponding to the reduction peaks can be found in the CV curves, revealing the excellent reversibility of the SnO_x/SiO_2 @N-CNF electrode. The small peaks at 0.67, 0.76 and 0.82 V can be linked to the stepwise de-alloying reaction of Li_xSn for Li^+ acquisition. The strong broad peak at 1.19 V in the first sweep, which then shifts to around 1.35 V in the second to fifth cycles, corresponds with the oxidation of Sn ($Sn + 2Li_2O \rightarrow SnO_2 + 4Li^+ + 4e^-$). Besides, the weak broad peak at around 0.5 V correspond to the delithiation process of Si ($Li_xSi \rightarrow Si + xLi^+ + xe^-$) [8]. Additionally, the CV curves in the 2–5 cycles are in highly accordance, which indicates the reversible of the electrochemical reactions in the SnO_x/SiO_2 @N-CNF electrodes. As shown in Fig. 6b, the electrochemical reactions found in CV curves are in great agreement with the plateaus in Fig. 5d. Besides, the 1st to 5th discharge-charge profiles also show excellent superposition, which can be a further proof of the reversibility and stability of the SnO_x/SiO_2 @ N-CNF electrode.

The capacitive mechanism and reaction kinetics for energy storage of the SnO_x/SiO_2@N-CNF electrode were further analyzed to gain thorough insights into the high specific capacity. As previously reported, there are two mechanisms of lithium storage in different electrode materials. One is diffusion-controlled process, which incorporates the contribution of the intercalation, conversion and alloying of Li ions. The other is capacitive-controlled process, which includes pseudocapacitive contribution from redox reactions on the

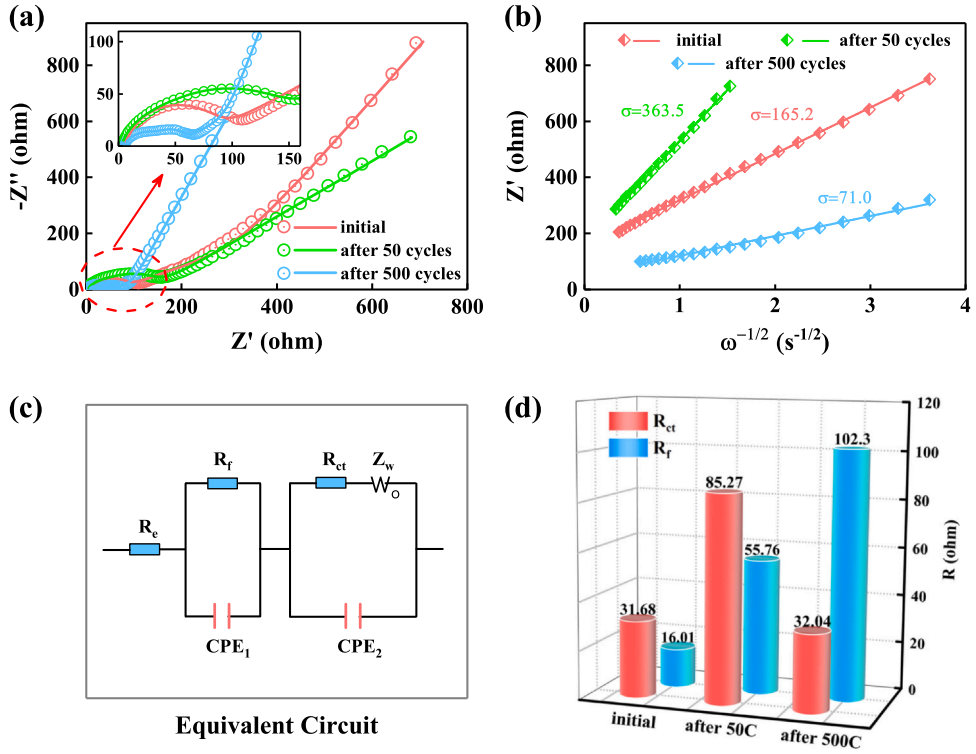

Fig. 7. (a) The electrochemical impedance spectra (symbol) and the fitting curves (line) and (b) the relationship plots between Z' and $\omega^{-1/2}$ in the low frequency range of the SnO_x/SiO_2@N-CNF electrode for initial, after 50 and 500 cycles. The insert figure is an enlargement of the circled part. (c) The equivalent circuit used in EIS. (d) The fitted value of R_{ct} and R_f .

surface of the active materials and the contribution of electrical double-layer. The CV curves at different sweeping rates from 0.1 to 1 mV/s are displayed in Fig. 6c, from which the energy storage kinetics of the SnO_x/SiO_2@N-CNF electrode could be analyzed more in-depth. As is reported, the charge storage and the current response at fixed potentials can be described as the power-law relationship:

$$i = k_1\nu^{1/2} + k_2\nu = a\nu^b \quad (1)$$

Here, i is the current at the fixed potential, ν is the scan rate, a and b are appropriate parameters, and $k_1\nu^{1/2}$ and $k_2\nu$ represent the diffusion-controlled and the surface capacitive contribution of the current, respectively [49]. As a result, the value of a and b can be easily calculated by fitting the functional relation curve of log(ν) and log(i) according to the above relationship. It is commonly recognized that the charge transfer process is dominated by the diffusion of Li ions when the value of b approaches 0.5, and dominated by the surface capacitance when it is near 1.0 [50]. The fitting results of the log(ν)-log(i) plot is exhibited in Fig. 6d to gain the b value. The values of b corresponding to the currents of the cathodic reduction peak at ~ 0.1 V and the anodic oxidation peak of Sn to SnO_2 in ~ 1.2–1.8 V are calculated to be 0.53 and 0.46, respectively. This result demonstrates that the process of energy conversion by lithium storage is a diffusion-controlled redox reaction process, which is relatively rare in previous studies.

Since the lithium storage mechanism of the SnO_x/SiO_2@N-CNF electrode is diffusion-dominant, it is of vital importance to further inquire into the lithium ion diffusion process and electrochemical conductivity. Hence, electrochemical impedance spectroscopy (EIS) analysis was conducted using the initial cell and the cell after 50 and 500 GDC cycles at 0.5 A/g, respectively. As shown in Fig. 7a, two semicircles and a diagonal can be observed in the Nyquist plots of all the three cells, where the suppressive semicircle in the high frequency region is related to the diffusion resistance of Li^+ through the SEI layer (R_f), the semicircle in the intermediate frequency region corresponds to the charge transfer resistance (R_{ct}) on the interface of electrode and electrolyte, and the diagonal in the low frequency region is associated with the Warburg impedance (Z_w) [49]. The plot of the cell after 50 cycles is quite similar to the initial cell, which further demonstrates the cyclic stability of the SnO_x/SiO_2 @N-CNF electrode. As we know, the Z_w in the low frequency region is closely related to the diffusion process of lithium ions. The value of the resistance (Z') in this range can be expressed as:

$$Z' = R_{ct} + R_{el} + \sigma\omega^{-1/2} \quad (2)$$

where R_{el} represents the electrolyte resistance, ω is the angular frequency, and σ is the Warburg factor related to the lithium ion diffusion coefficient, respectively [45]. Fig. 7b shows the plots and the fitting curves of Z'-$\omega^{-1/2}$ of the three cells, from which the value of σ can be obtained as 165.2, 363.5 and 71.0 $\Omega\,s^{-1/2}$, respectively. Therefore, the diffusion coefficient (D) of the lithium ions can be obtained in the light of the following equation:

$$D = \frac{R^2T^2}{2A^2n^4F^4C^2\sigma^2} \quad (3)$$

where R, T and F are three constant: universal gas constant (8.314 J mol^{-1} K^{-1}), absolute temperature (298.15 K) and Faraday constant (96486 C/mol), respectively. Also, the parameter n corresponds to the number of the transferred charge during redox process, A is the total area of the tested electrode surface (cm^2) and C is the molar concentration of lithium ions (mol/cm^3) [51]. As a result, the Li^+ diffusion coefficient of the cell after 500 cycles was calculated as 5.50×10^{-12} cm^2/s, which is much higher than the cell after 50 cycles (2.10×10^{-13} cm^2/s) and a little higher than the initial cell (1.02×10^{-12} cm^2/s). It indicates that the diffusion of the lithium ions was becoming weaker during the first several cycles due to the obstruction of the SEI layer. Nevertheless, with the continuous charging and discharging, the diffusion of lithium ions is gradually accelerated. This can be attributed to the slow formation of a uniform

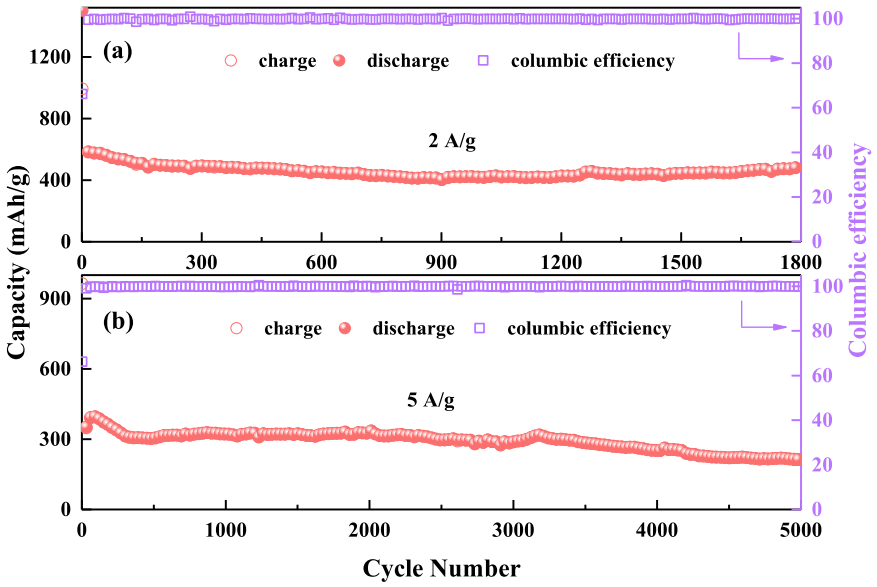

Fig. 8. Long-term cycling performance of the SnO_x/SiO_2@N-CNF electrode (a) at 2 A/g for 1800 cycles and (b) 5 A/g for 5000 cycles, 0.1 A/g for the first five cycles.

Li_2O matrix during the charge-discharge process. It has been reported that the aggregation of the Li_xSn particles could be prevented by the Li_2O matrix, which leads to shorter diffusion path of lithium ions [52]. Because of the synergistic effect of SiO_2 and SnO_x, the formation of the lithium oxide in the SnO_x/SiO_2 @N-CNF electrode is partially reversible, leading to a slow formation of the uniform Li_2O matrix, and thereby improving the lithium ion diffusion [45]. Fig. 7c displays the equivalent circuit used in Fig. 7a to fit, where R_e is the source resistance that results in the intercept on the Z' axis in the high frequency region. Fig. 7d precisely presents the fitted values of R_f and R_{ct} for the three cells, demonstrating that the transfer resistance of the Li^+ through the SEI layer was increasing continually with the cycling process. Nevertheless, the charge transfer resistance increased after 50 cycles and decreased after 500 cycles, which could also be attributed to the formation of the uniform Li_2O matrix. The Li_2O matrix can prevent the Li_xSn particles from aggregation, and thereby providing large surface area for redox reaction, so the charge transfer could be promoted. To further prove that it is caused by the synergistic effect of SiO_2 and SnO_x, the EIS spectra and the fitted R_{ct} and R_f value of the SnO_x@N-CNF electrode for initial, after 50 and 500 cycles are shown in Fig. S6. The value of the fitted R_{ct} for SnO_x@N-CNF decreased continually with the cycling process and there is no trend of first increasing and then decreasing. That may be due to the formation of ultrafine nanocrystals during the cycling process, instead of forming a uniform Li_2O matrix. Therefore, this can also be a side evidence of synergistic effect between SiO_2 and SnO_x.

Inspired by the above intriguing electrochemical performance analysis, further long-term cycle performance were tested at higher current density of 2 A/g and 5 A/g, as shown in Fig. 8. Unsurprisingly, both the two capacity curves of the SnO_x/SiO_2@N-CNF electrode for long-term cycling remain remarkably steady. The specific capacity of SnO_x/SiO_2@N-CNF maintained around 480 mAh/g at 2 A/g after 1800 cycles of charge and discharge with 82.8% capacity retention. What's more, it could also maintain around 300 mAh/g even after 3000 cycles at a ultrahigh current density of 5 A/g with 81.1% capacity retention. Although the capacity was slowly decreasing after charging and discharging for 3000 cycles, it remained above 200 mAh/g after 5000 cycles. These results further prove that the SnO_x/SiO_2@N-CNF composite with a unique structure, that the ultrafine SnO_x and SiO_2 nanoparticles are encapsulated in the N-CNFs, shows remarkable advantage in cycling stability. Besides, the columbic efficiency was remain above 99.5% throughout the cycling process at the both current densities. At these current density, the charging process is extremely fast, which is at most only 14 min at 2 A/g and 4 min at 5 A/g. Hence, the SnO_x/SiO_2@N-CNF composite could be employed in the lithium-ion battery quick-acting charging technology. Furthermore, the long-term cycle performance of the SnO_x/SiO_2@N-CNF electrode is in excess of most anode materials based on carbon group owing to the synergistic effect of SnO_x, SiO_2 and N-CNFs [53,54]. Table 1 lists the comparison of the cycling stability of the SnO_x/SiO_2 @N-CNF electrode in this work and that of the reported relevant anode materials recently. It indicates that both the specific capacities and the cycling numbers of the SnO_x/SiO_2@N-CNF electrode in this work are superior at the current densities of 1, 2 and 5 A/g, respectively. Therefore, the SnO_x/SiO_2@N-CNF composite with durable lifespan at high current densities could be an excellent candidate material for the anode of LIBs, especially for quick-acting charging technology.

Consequently, the composite of hydrothermal ultrafine SnO_x nanoparticles and electrospinning SiO_2@N-CNF delivers enhanced rate and cyclic performance compared to SnO_2, SiO_2@N-CNF and SnO_x@N-CNF, which could provide a new design strategy of the anode materials for the lithium-ion battery quick-acting charging

Table 1
The cycling performance comparison of the SnO_x/SiO_2 @N-CNF electrode and previously reported carbon group based anode materials.

Materials	Rate (A/g)	Capacity (mAh/g)	Cycles (times)	Ref.
Si/SiO_x@CNF	3	470	1000	[7]
SiO_2-TiO_2@C	1	700	600	[8]
SnO_2/Sn-rGO	1.6	512	400	[9]
SnO_2@OMC	5	321	1000	[10]
c-SnO_2@3D-CNT	1	452	500	[14]
SiO_x@G	1	661	1000	[30]
SnO_2 QDs@GF	5	320	1000	[31]
SnO_2/Sn-rGO	1.6	170	970	[34]
C@SnO_2-rGO-SnO_2	1	703	1200	[40]
TiO_2-Sn@CNF	0.2	643	1100	[43]
SnSe/SnO_x@CNF	1	345	1000	[46]
W-SnO_2@GO	1	720	2000	[48]
h-SnO_2/N-rGO	1	652	200	[53]
C/SnO_2/Sn	1	504	1000	[54]
SnO_x/SiO_2@N-CNF	**1**	**754**	**1000**	**This work**
	2	**480**	**1800**	
	5	**300**	**3000**	

technology. On the basis of the above results and discussion, the remarkable performance of lithium storage can be attributed to the synergy effect of the ultrafine SnO_x and SiO_2 nanoparticles and the N-CNFs in the following aspects: (1) The unique 1D structure that the N-CNFs wrapped the ultrafine SnO_x and SiO_2 nanoparticles can efficiently block the direct contact of the SnO_x and SiO_2 with electrolyte, thereby reducing the secondary reaction and prevent the particle aggregation. Also, the SnO_x and SiO_2 nanoparticles were encapsulate in the N-CNFs, so the volume variations could be confined during lithiation/delithiation process. Therefore, the cycling stability was significantly improved due to the especially stable structure. (2) The specific capacity was improved by the SnO_x and SiO_2 with inherent high theoretical capacity owing to the contribution of conversion-alloying reaction. (3) The 1D structural N-CNFs could shorten the diffusion path of the lithium ions, indeed accelerating the Li^+ diffusion. Thus, the rate performance and the electrical conductivity were remarkably improved. (4) Last but not least, the synergistic effect of SnO_x and SiO_2 promoted the formation of the partially reversible lithium oxide, forming a uniform Li_2O matrix gradually, and thereby improving the lithium ion diffusion. As a result, the SnO_x/SiO_2@N-CNF electrode delivered a diffusion-controlled capacitive mechanism.

4. Conclusion

In conclusion, a novel composite of hydrothermally synthesized ultrafine SnO_x nanoparticles and SiO_2@N-CNF was fabricated via electrospinning technique and subsequent annealing treatment. The SnO_x and SiO_2 nanoparticles were firmly encapsulated in the N-CNFs forming a especially stable structure. The N-CNFs can not only prevent the volume expansion and the direct contact with electrolyte of SnO_x and SiO_2, but also improve electrical conductivity by shorten the carrier transport path. Moreover, the synergistic effect of SnO_x and SiO_2 could improve the lithium ion diffusion of the SnO_x/SiO_2@ N-CNF electrode, resulting in a diffusion-controlled capacitive mechanism. As a consequence, the SnO_x/SiO_2@N-CNF delivers extraordinary rate performance, remarkable long-term cycling performance at high current density and high electrical conductivity as the anode material of LIBs. This work could provide a new design strategy of the anode materials for the lithium-ion battery quick-acting charging technology.

CRediT authorship contribution statement

Liyuan Ao: Conceptualization, Validation, Formal analysis, Writing – original draft preparation. **Shenyu Du:** Methodology, Formal analysis. **Jiaxuan Yang:** Methodology. **Chunqiao Jin:** Formal analysis. **Kai Jiang:** Formal analysis, Supervision. **Liyan Shang:** Methodology, Formal analysis. **Yawei Li:** Formal analysis. **Jinzhong Zhang:** Methodology, Formal analysis. **Liangqing Zhu:** Formal analysis. **Zhigao Hu:** Writing – review & editing, Supervision, Project administration, Funding acquisition. **Junhao Chu:** Funding acquisition.

Declaration of Competing Interest

The authors declare that they have no known competing financial interests or personal relationships that could have appeared to influence the work reported in this paper.

Acknowledgment

This work was financially supported by the National Natural Science Foundation of China (Grant Nos. 91833303, 61974043, 62074058, 62090013 and 61974044), the National Key Research and Development Program of China (Grant No. 2019YFB2203403), the Projects of Science and Technology Commission of Shanghai Municipality (Grant Nos. 18JC1412400, 18YF1407200, 18YF1407000 and 19511120100), the Program for Professor of Special Appointment (Eastern Scholar) at Shanghai Institutions of Higher Learning and Shanghai Pujiang Program (20PJ1403600).

Appendix A. Supporting information

Supplementary data associated with this article can be found in the online version at doi:10.1016/j.jallcom.2021.162703.

References

[1] M. Armand, J.M. Tarascon, Building better batteries, Nature 451 (2008) 652–657, https://doi.org/10.1038/451652a
[2] A.S. Aricó, P. Bruce, B. Scrosati, J.M. Tarascon, W. Van Schalkwijk, Nanostructured materials for advanced energy conversion and storage devices, Nat. Mater. 4 (2005) 366–377, https://doi.org/10.1038/nmat1368
[3] C.K. Chan, H.L. Peng, G. Liu, K. McIlwrath, X.F. Zhang, R.A. Huggins, Y. Cui, High-performance lithium battery anodes using silicon nanowires, Nat. Nanotechnol. 3 (2008) 31, https://doi.org/10.1038/nnano.2007.411
[4] T.H. Kim, J.S. Park, S.K. Chang, S. Choi, J.H. Ryu, H.K. Song, The current move of lithium ion batteries towards the next phase, Adv. Energy Mater. 2 (2012) 860–872, https://doi.org/10.1002/aenm.201200028
[5] D. Chao, C. Zhu, P. Yang, X. Xia, J. Liu, J. Wang, X. Fan, S.V. Savilov, J. Lin, H.J. Fan, Z.X. Shen, Array of nanosheets render ultrafast and high-capacity Na-ion storage by tunable pseudocapacitance, Nat. Commun. 7 (2016) 12122, https://doi.org/10.1038/ncomms12122
[6] S.Q. Zhao, Z.W. Wang, Y.J. he, H.R. Jiang, Y.W. Harn, X.Q. Liu, C.L. Su, H.L. Jin, Y. Li, S. Wang, Q. Shen, Z.Q. Lin, A robust route to $Co_2(OH)_2CO_3$ ultrathin nanosheets with superior lithium storage capability templated by aspartic acid-functionalized graphene oxide, Adv. Energy Mater. 9 (2019) 1901093, https://doi.org/10.1002/aenm.201901093
[7] W.J. Zhang, Y.Q. Weng, W.C. Shen, R.T. Lv, F.Y. Kang, Scalable synthesis of lotus-seed-pod-like Si/SiO_x @CNF: applications in freestanding electrode and flexible full lithium-ion batteries, Carbon 158 (2020) 163–171, https://doi.org/10.1016/j.carbon.2019.11.092
[8] Z.L. Li, H.L. Zhao, P.P. Lv, Z.J. Zhang, Y. Zhang, Z.H. Du, Y.Q. Teng, L.N. Zhao, Z.M. Zhu, Watermelon-like structured SiO_x -TiO_2 @C nanocomposite as a high-performance lithium-ion battery anode, Adv. Funct. Mater. 28 (2018) 1605711, https://doi.org/10.1002/adfm.201605711
[9] X.Y. Sui, X.K. Huang, Y.P. Wu, R. Ren, H.H. Pu, J.B. Chang, G.H. Zhou, S. Mao, J.H. Chen, Organometallic precursor-derived SnO_2 /Sn-reduced graphene oxide sandwiched nanocomposite anode with superior lithium storage capacity, ACS Appl. Mater. Interfaces 10 (2018) 26170–26177, https://doi.org/10.1021/acsami.8b04851
[10] D.D. Liu, Z.Y. Wei, L.M. Liu, H. Pan, X.M. Duan, L. Xia, B. Zhong, H.T. Wang, D.C. Jia, Y. Zhou, X.X. Huang, Ultrafine SnO_2 anchored in ordered mesoporous carbon framework for lithium storage with high capacity and rate capability, Chem. Eng. J. 406 (2021) 126710, https://doi.org/10.1016/j.cej.2020.126710
[11] S.Q. Zhao, C.D. Sewell, R.P. Liu, S.R. Jia, Z.W. Wang, Y.J. He, K.J. Yuan, H.L. Jin, S. Wang, X.Q. Liu, Z.Q. Lin, SnO_2 as advanced anode of alkali-ion batteries: inhibiting Sn coarsening by crafting robust physical barriers, void boundaries, and heterophase interfaces for superior electrochemical reaction reversibility, Adv. Energy Mater. 10 (2020) 1902657, https://doi.org/10.1002/aenm.201902657
[12] F.L. Wang, G. Chen, N. Zhang, X.H. Liu, R.Z. Ma, Engineering of carbon and other protective coating layers for stabilizing silicon anode materials, Carbon Energy 1 (2019) 219–245, https://doi.org/10.1002/cey2.24
[13] J.X. Wu, Y.L. Cao, H.M. Zhao, J.F. Mao, Z.P. Guo, The critical role of carbon in marrying silicon and graphite anodes for high-energy lithium-ion batteries, Carbon Energy 1 (2019) 57–76, https://doi.org/10.1002/cey2.2
[14] X.W. Li, Z.B. Yang, S.M. Lin, D. Li, H.W. Yue, X.N. Shang, Y.J. Fu, D.Y. He, A facile and inexpensive approach to improve the performance of silicon film as an anode for lithium ion batteries, J. Mater. Chem. A 2 (2014) 14817–14821, https://doi.org/10.1039/c4ta03304c
[15] P. Bhattacharya, J.H. Lee, K.K. Kar, H.S. Park, Carambola-shaped SnO_2 wrapped in carbon nanotube network for high volumetric capacity and improved rate and cycle stability of lithium ion battery, Chem. Eng. J. 369 (2019) 422–431, https://doi.org/10.1016/j.cej.2019.03.022
[16] H.J. Wang, X.Y. Jiang, Y. Chai, X. Yang, R. Yuan, Sandwich-like C@SnO_2 /Sn/void@C hollow spheres as improved anode materials for lithium ion batteries, J. Power Sources 379 (2018) 191–196, https://doi.org/10.1016/j.jpowsour.2018.01.054
[17] B.B. Jiang, Y.J. He, B. Li, S.Q. Zhao, S. Wang, Y.B. He, Z.Q. Lin, Polymer-templated formation of polydopamine-coated SnO_2 nanocrystals: anodes for cyclable lithium-ion batteries, Angew. Chem. Int. Ed. 56 (2017) 1869–1872, https://doi.org/10.1002/anie.201611160
[18] Y. Jiang, Y.Y. Wan, W. Jiang, H.H. Tao, W.R. Li, S.S. Huang, Z.W. Chen, B. Zhao, Stabilizing the reversible capacity of SnO_2 /graphene composites by Cu nanoparticles, Chem. Eng. J. 367 (2019) 45–54, https://doi.org/10.1016/j.cej.2019.02.141

[19] L. Yang, T. Dai, Y.C. Wang, D.G. Xie, R.L. Narayan, J. Li, X.H. Ning, Chestnut-like SnO_2 /C nanocomposites with enhanced lithium ion storage properties, Nano Energy 5 (2016) 885–891, https://doi.org/10.1016/j.nanoen.2016.08.060

[20] J.L. Wu, J.H. Liu, Z. Wang, X.Z. Gong, Y. Wang, A new design for Si wears double jackets used as a high-performance lithium-ion battery anode, Chem. Eng. J. 370 (2019) 565–572, https://doi.org/10.1016/j.cej.2019.03.253

[21] J. Han, D. Kong, W. Lv, D.M. Tang, D. Han, C. Zhang, D. Liu, Z. Xiao, X. Zhang, J. Xiao, X. He, F.C. Hsia, C. Zhang, Y. Tao, D. Golberg, F. Kang, L. Zhi, Q.H. Yang, Caging tin oxide in three-dimensional graphene networks for superior volumetric lithium storage, Nat. Commun. 9 (2018) 402, https://doi.org/10.1038/s41467-017-02808-2

[22] M. Yousaf, Y.S. Wang, Y.J. Chen, Z.P. Wang, Y.J. Chen, Z.P. Wang, W. Aftab, A. Mahmood, W. Wang, S.J. Guo, R.P.S. Han, Tunable free-standing core?shell CNT@$MoSe_2$ anode for lithium storage, ACS Appl. Mater. Interfaces 10 (2018) 14622–14631, https://doi.org/10.1021/acsami.7b19739

[23] W.J. Dong, J.J. Xu, C. Wang, Y. Lu, X.Y. Liu, X. Wang, X.T. Yuan, Z. Wang, T.Q. Lin, M.L. Sui, I.W. Chen, F. Huang, A robust and conductive black tin oxide nanostructure makes efficient lithium-ion batteries possible, Adv. Mater. 29 (2017) 1700136, https://doi.org/10.1002/adma.201700136

[24] Q.L. Wei, F.Y. Xiong, S.S. Tan, L. Huang, E.H. Lan, B. Dunn, L.Q. Mai, Porous one-dimensional nanomaterials: design, fabrication and applications in electrochemical energy storage, Adv. Mater. 29 (2017) 1602300, https://doi.org/10.1002/adma.201602300

[25] R.Z. Chen, Y. Hu, Z. Shen, P. Pan, X. He, K.S. Wu, X.W. Zhang, Z.L. Cheng, Facile fabrication of foldable electrospun polyacrylonitrile-based carbon nanofibers for flexible lithium-ion batteries, J. Mater. Chem. A 5 (2017) 12914–12921, https://doi.org/10.1039/c7ta02528a

[26] S.J. Peng, L.L. Li, J.K.Y. Lee, L.L. Tian, M. Srinivasan, S. Adams, S. Ramakrishna, Electrospun carbon nanofibers and their hybrid composites as advanced materials for energy conversion and storage, Nano Energy 22 (2016) 361–395, https://doi.org/10.1016/j.nanoen.2016.02.001

[27] J.W. Jung, C.L. Lee, S. Yu, I.D. Kim, Electrospun nanofibers as a platform for advanced secondary batteries: a comprehensive review, J. Mater. Chem. A 4 (2016) 703–750, https://doi.org/10.1039/c5ta06844d

[28] L.P. Yang, Y.E. Zhu, J. Sheng, F. Li, B. Tang, Y. Zhang, Z. Zhou, T-Nb_2 O_5 /C nanofibers prepared through electrospinning with prolonged cycle durability for high-rate sodium-ion batteries induced by pseudocapacitance, Small 13 (2017) 1702588, https://doi.org/10.1002/smll.201702588

[29] Y. Sun, Y. Liu, Y.D. Zheng, Z.J. Li, J. Fan, L. Wang, X.Q. Liu, J. Liu, W. Shou, Enhanced energy harvesting ability of ZnO/PAN hybrid piezoelectric nanogenerators, ACS Appl. Mater. Interfaces 12 (2020) 54936–54945, https://doi.org/10.1021/acsami.0c14490

[30] Q. Xu, J.K. Sun, P. Yang, Z.L. Yu, Y.X. Yin, S. Xin, S.H. Yu, Y.G. Guo, SiO_x encapsulated in graphene bubble film: an ultrastable li-ion battery anode, Adv. Mater. 30 (2018) 1001430, https://doi.org/10.1002/adma.201707430

[31] L. Gao, G.S. Wu, J. Ma, T.C. Jiang, B. Chang, Y.S. Huang, S. Han, SnO_2 quantum dots@graphene framework as a high-performance flexible anode electrode for lithium-ion batteries, ACS Appl. Mater. Interfaces 12 (2020) 12982–12989, https://doi.org/10.1021/acsami.9b22679

[32] L.Y. Ao, C. Wu, X. Wang, Y.N. Xu, K. Jiang, L.Y. Shang, Y.W. Li, J.Z. Zhang, Z.G. Hu, J.H. Chu, Superior and reversible lithium storage of SnO_2 /graphene composites by silicon doping and carbon sealing, ACS Appl. Mater. Interfaces 12 (2020) 20824–20837, https://doi.org/10.1021/acsami.0c00073

[33] H.G. Wang, Q. Wu, Y.H. Wang, X. Wang, L.L. Wu, S.Y. Song, H.J. Zhang, Molecular engineering of monodisperse SnO_2 nanocrystals anchored on doped graphene with high-performance lithium/sodium-storage properties in half/full cells, Adv. Energy Mater. 9 (2018) 1802993, https://doi.org/10.1002/aenm.201802993

[34] L. David, R. Bhandavat, U. Barrera, G. Singh, Silicon oxycarbide glass-graphene composite paperelectrode for long-cycle lithium-ion batteries, Nat. Commun. 8 (2016) 10998, https://doi.org/10.1021/acsami.6b00107

[35] X. Wu, X.H. Liang, X.F. Zhang, L.X. Lan, S. Li, Q.X. Gai, Structural evolution of plasma sprayed amorphous Li_4 Ti_5 O_{12} electrode and ceramic/polymer composite electrolyte during electrochemical cycle of quasi-solid-state lithium battery, J. Adv. Ceram. 10 (2021) 347–354, https://doi.org/10.1007/s40145-020-0447-9

[36] L.M Liu, X.X Huang, Z.Y Wei, X.M Daun, B Zhong, L Xia, T Zhang, H.T Wang, D.C Jia, Y Zhou, R Zhang, Solvents adjusted pure phase CoCO3 as anodes for high cycle stability, J. Adv. Ceram. 10 (2021) 509–519.

[37] H.Y. He, W. Fu, H.T. Wang, H. Wang, C.H. Jin, H.J. Fan, Z. Liu, Silica-modified, SnO_2 -graphene "slime" for self-enhanced li-ion battery anode, Nano Energy 34 (2017) 449–455, https://doi.org/10.1016/j.nanoen.2017.03.017

[38] B.K. Cao, Z.Q. Liu, C.Y. Xu, J.T. Huang, H.T. Fang, Y. Chen, High-rate-induced capacity evolution of mesoporous C@SnO_2 @C hollow nanospheres for ultra-long cycle lithium-ion batteries, J. Power Sources 414 (2019) 233–241, https://doi.org/10.1016/j.jpowsour.2019.01.001

[39] S. Paneliya, S. Khanna, Utsav, A.P. Singh, Y.K. Patel, A. Vanpariya, N.H. Makani, R. Banerjee, I. Mukhopadhyay, Core shell paraffin/silica nanocomposite: a promising phase change material for thermal energy storage, Renew. Energ. 167 (2021) 591–599, https://doi.org/10.1016/j.renene.2020.11.118

[40] W.Q. Yao, S.B. Wu, L. Zhang, Y.L. Wang, Two-dimensional porous carbon-coated sandwich-like mesoporous SnO_2 /graphene/mesoporous SnO_2 nanosheets towards high-rate and long cycle life lithium-ion batteries, Chem. Eng. J. 361 (2019) 329–341, https://doi.org/10.1016/j.cej.2018.08.217

[41] N.N. Hu, X.S. Lv, Y. Dai, L.L. Fan, D.B. Xiong, X.F. Li, SnO_2 /reduced graphene oxide interlayer mitigating the shuttle effect of Li-S batteries, ACS Appl. Mater. Interfaces 10 (2018) 18665–18674, https://doi.org/10.1021/acsami.8b03255

[42] J. Lee, A. Urban, X. Li, D. Su, G. Hautier, G. Ceder, Unlocking the potential of cation-disordered oxides for rechargeable lithium batteries, Science 343 (2014) 519–522, https://doi.org/10.1126/science.1246957

[43] M.L. Mao, F.L. Yan, C.Y. Cui, J.M. Ma, M. Zhang, T.H. Wang, C.S. Wang, Pipe-wire TiO_2 -Sn@carbon nanofibers paper anodes for lithium and sodium ion batteries, Nano Lett. 17 (2017) 3830–3836, https://doi.org/10.1021/acs.nanolett.7b01152

[44] C. Zhu, X. Xia, J. Liu, Z. Fan, D. Chao, H. Zhang, H.J. Fan, TiO_2 nanotube@SnO_2 nanoflake core-branch arrays for lithium-ion battery anode, Nano Energy 4 (2014) 105–112, https://doi.org/10.1016/j.nanoen.2013.12.018

[45] Y.Z. Tan, K.W. Wong, K.M. Ng, Novel silicon doped tin oxide-carbon microspheres as anode material for lithium ion batteries: the multiple effects exerted by doped Si, Small 13 (2017) 1702614, https://doi.org/10.1002/smll.201702614

[46] H.C. Yuan, Y.Q. Jin, J.L. Lan, Y. Liu, Y.H. Yu, H.P. Yang, In situ synthesized SnSe nanorods in a SnO_x @CNF membrane toward high-performance freestanding and binder-free lithium-ion batteries, Inorg. Chem. Front 5 (2018) 932–938, https://doi.org/10.1039/c7qi00762k

[47] H.C. Yuan, Y.Q. Jin, J.L. Lan, Y. Liu, Y.H. Yu, H.P. Yang, Honeycomb-inspired design of ultrafine SnO_2 @C nanospheres embedded in carbon film as anode materials for high performance lithium- and sodium-ion battery, J. Power Sources 359 (2017) 340–348, https://doi.org/10.1016/j.jpowsour.2017.05.064

[48] S. Wang, L.Y. Shi, G.R. Chen, C.Q. Ba, Z.Y. Wang, J.F. Zhu, Y. Zhao, M.H. Zhang, S. Yuan, In situ synthesis of tungsten-doped SnO_2 and graphene nanocomposites for high-performance anode materials of lithium-ion batteries, ACS Appl. Mater. Interfaces 9 (2017) 17163–17171, https://doi.org/10.1021/acsami.7b03705

[49] J.Y. Wang, C. Wu, Q.L. Deng, K. Jiang, L.Y. Shang, Z.G. Hu, J.H. Chu, Highly durable and cycle-stable lithium storage based on MnO nanoparticle-decorated 3D interconnected CNT/graphene architecture, Nanoscale 10 (2018) 13140–13148, https://doi.org/10.1039/c8nr01835a

[50] M.J. Li, Q.L. Deng, J.Y. Wang, K. Jiang, Z.G. Hu, J.H. Chu, In situ carbon encapsulation of vertical MoS_2 arrays with SnO_2 for durable high rate lithium storage: dominant pseudocapacitive behavior, Nanoscale 10 (2018) 741–751, https://doi.org/10.1039/c7nr07359c

[51] Y.Q. Qiao, W.L. Feng, J. Li, T.D. Shen, Ultralong cycling stability of carbon-nanotube/$LiFePO_4$ nanocomposites as electrode materials for lithium-ion batteries, Electrochim. Acta 232 (2017) 323–331, https://doi.org/10.1016/j.electacta.2017.02.161

[52] J. Xie, N. Imanishi, A. Hirano, Y. Takeda, O. Yamamoto, X.B. Zhao, G.S. Cao, Li-ion diffusion behavior in Sn, SnO and SnO_2 thin films studied by galvanostatic intermittent titration technique, Solid State Ion. 181 (2010) 1611–1615, https://doi.org/10.1016/j.ssi.2010.09.006

[53] N. Wu, W. Du, X. Gao, L. Zhao, G. Liu, X. Liu, H. Wu, Y.B. He, Hollow SnO_2 nanospheres with oxygen vacancies entrapped by a N-doped graphene network as robust anode materials for lithium-ion batteries, Nanoscale 10 (2018) 11460–11466, https://doi.org/10.1039/c8nr02290a

[54] Y. Cheng, Z. Yi, C. Wang, Y. Wu, L. Wang, Controllable fabrication of C/Sn and C/SnO/Sn composites as anode materials for high-performance lithium-ion batteries, Chem. Eng. J. 330 (2017) 1035–1043, https://doi.org/10.1016/j.cej.2017.08.066